nature communications

Article

https://doi.org/10.1038/s41467-025-56195-0

High-entropy engineered $BaTiO_3$-based ceramic capacitors with greatly enhanced high-temperature energy storage performance

Received: 21 July 2024

Accepted: 13 January 2025

Published online: 21 January 2025

Check for updates

Xi Kong[1], Letao Yang[1,2] ✉, Fanqi Meng[1], Tao Zhang[3], Hejin Zhang[3], Yuan-Hua Lin[1], Houbing Huang[2], Shujun Zhang[4], Jinming Guo[3] ✉ & Ce-Wen Nan[1] ✉

Ceramic capacitors with ultrahigh power density are crucial in modern electrical applications, especially under high-temperature conditions. However, the relatively low energy density limits their application scope and hinders device miniaturization and integration. In this work, we present a high-entropy $BaTiO_3$-based relaxor ceramic with outstanding energy storage properties, achieving a substantial recoverable energy density of 10.9 J/cm^3 and a superior energy efficiency of 93% at applied electric field of 720 kV/cm. Of particular importance is that the studied high-entropy composition exhibits excellent energy storage performance across a wide temperature range of −50 to 260 °C, with variation below 9%, additionally, it demonstrates great cycling reliability at 450 kV/cm and 200 °C up to 10^6 cycles. Electrical and in-situ structural characterizations revealed that the high-entropy engineered local structures are highly stable under varying temperature and electric fields, leading to superior energy storage performance. This study provides a good paradigm of the efficacy of the high-entropy engineering for developing high-performance dielectric capacitors.

Ceramic capacitors are widely used in electronic and electrical devices and circuits due to their irreplaceable functions such as coupling/decoupling, dc-blocking, power functioning, and energy storage[1,2]. Although barium titanate ($BaTiO_3$)-based ceramic capacitors have been extensively used in the above fields, they are facing challenges from some booming high-temperature applications such as electric vehicles, deep-well gas exploration, and aerospace power electronics, which require capacitors to operate reliably in an environment exceeding 150 °C[3–5]. One of the key factors preventing $BaTiO_3$-based capacitors from working at high temperatures is the low Cuire temperature (~130 °C for unmodified $BaTiO_3$)[6], where the dielectric properties and capacitance change dramatically[6]. While most additives in $BaTiO_3$-based dielectrics lower the Curie temperature, further worsening the high-temperature energy storage performance[6].

One possible solution for this issue is adopting relaxor ceramics, which possess temperature-insensitive dielectric constant over a wide temperature range due to their diffuse phase transition[7–10]. Of particular significance is that relaxors typically exhibit slim polarization-

[1]State Key Laboratory of New Ceramics and Fine Processing, School of Materials Science and Engineering, Tsinghua University, Beijing, China. [2]Advanced Research Institute of Multidisciplinary Science, Beijing Institute of Technology, Beijing, China. [3]Electron Microscopy Center, Ministry-of-Education Key Laboratory of Green Preparation and Application for Functional Materials, School of Materials Science and Engineering, Hubei University, Wuhan, China. [4]Institute for Superconducting and Electronic Materials, Faculty of Engineering and Information Sciences, University of Wollongong, Wollongong, New South Wales, Australia. ✉e-mail: ltyang@bit.edu.cn; guojinming@hubu.edu.cn; cwnan@mail.tsinghua.edu.cn

electric field loops (*P-E* loops) associated with the highly dynamic polar nanoregions (PNRs), leading to both high recoverable energy density (W_{rec}) and high energy efficiency (η)[7–9,11]. The relaxor characteristics in $BaTiO_3$ can be induced by replacing Ba^{2+}, Ti^{4+}, or both with homovalent or heterovalent cations. For homovalent substitution, such as $(Ba_{1-x}Sr_x)TiO_3$[12], $Ba(Ti_{1-x}Zr_x)O_3$[13], and $Ba(Ti_{1-x}Sn_x)O_3$[14], the crossover from normal ferroelectrics to relaxors occurrs at a relatively high substitution level (> 30%). For heterovalent substitutiton, on the other hand, forming solid solution between $BaTiO_3$ and other perovskite oxide end members is common. For example, $BaTiO_3$-$BiMO_3$ relaxors, where M represents one trivalent cation (e.g., Sc^{3+}) or more cations with a net trivalent equivalent (e.g., $(Mg_{1/2}Ti_{1/2})^{3+}$), have been actively studied[15]. One distinct feature of this class of relaxor is that the activation energies for PNR coupling are much higher than those of classical relaxors[15,16], which is attractive for energy storage applications as it prevents long-range dipole ordering under high electric fields, leading to field-insensitive dielectric constants and delayed polarization saturation[7,15,17]. Compared with homovalent substitution, more cations simultaneously replace the matrix cations in $BaTiO_3$, inducing relaxor characteristics at relatively low $BiMO_3$ concentration[15]. In some cases, such as $BaTiO_3$-$BiScO_3$[16], $BaTiO_3$-$Bi(Mg_{1/2}Ti_{1/2})O_3$[18], and $BaTiO_3$-$Bi(Zn_{1/2}Ti_{1/2})O_3$-$BiScO_3$[19], higher $BiMO_3$ content (≥ 40 mol%) results in temperature-stable dielectric plateaus and low dielectric loss at high temperatures, making these ceramics highly desirable for high-temperature energy storage capacitors.

When M^{3+} consists of two or more cation species such as $(Mg_{1/2}Ti_{1/2})^{3+}$, the $BaTiO_3$-$BiMO_3$ ceramics with high $BiMO_3$ content (≥ 40%) can be classified as high-entropy ceramics[20,21]. The configuration entropy (S_{config}) is defined as[21]:

$$S_{config} = -R\left(\sum_{i=1}^{N} x_i \ln x_i\right) + \left(\sum_{j=1}^{M} x_j \ln x_j\right) \quad (1)$$

where $N(M)$ and $x_i(x_j)$ represent element species and the mole fraction of elements present in cation(anion) sites, respectively. R is the universal gas content. Materials with S_{config} greater than 1.5 R are defined as high-entropy materials[21]. High-entropy design has been proven effective for improving energy storage performance of capacitors[22–29]. For example, by increasing S_{config} of $Bi_4Ti_3O_{12}$ Aurivillius thin films, a pyrochlore $Bi_2Ti_2O_7$-type phase was stabilized, which is thermodynamically unstable[22]. Furthermore, the lattice distorted nano-crystalline grains and a disordered amorphous-like phase introduced by the high-entropy design, contributed to enhanced breakdown strength and energy storage performance (W_{rec} = 182 J/cm^3). By adopting the high-entropy design and multilayer structure, both resistivity and polarization were enhanced, leading to a high W_{rec} of 16.6 J/cm^3 in $BaTiO_3$-$BiFeO_3$-$CaTiO_3$ ternary system[23]. Numerous ions with various radii and valence states were introduced in $(K_{0.2}Na_{0.8})NbO_3$ matrix to enhance S_{config} and form multiphase nanoclusters. The local stress and electric fields were enhanced due to the high-entropy strategy, resulting in improved W_{rec} of 10.06 J/cm^3 and η of 90.8% in this lead-free bulk ceramic[25]. In brief, high-entropy strategy can be used as a guide to develop dielectric materials with ultrahigh comprehensive energy storage properties.

In this work, $(1-x)(Ba_{0.8}Ca_{0.2})TiO_3$-$xBi(Mg_{0.5}Zr_{0.5})O_3$ (denoted as (100-100x)BCT20-100xBMZ) relaxor system with high $Bi(Mg_{0.5}Zr_{0.5})O_3$ content was designed to achieve temperature-stable dielectric constants and increase the S_{config} of the solid solution, both conducive to improve the energy storage performance, particularly at high temperatures and electric fields. Consequently, both high W_{rec} of 10.9 J/cm^3 and high η of 93% were achieved in the ceramics with x = 0.3 at 720 kV/cm and room temperature. Moreover, the ceramics exhibited a stable W_{rec} of 5.0 ± 0.5 J/cm^3 with η above 90% across a wide temperature range of −50–260 °C. The ceramics also demonstrated excellent reliability with minimal degradation in energy storage properties after cycling 10^6 times at 200 °C. This confirms that high-entropy engineering is an effective strategy for improving the high-temperature energy storage performance of $BaTiO_3$-$BiMO_3$ ceramics.

Results and discussion

Structural and electrical properties of (100-100x)BCT20-100xBMZ ceramics with varying configuration entropy

The XRD patterns of (100-100x)BCT20-100xBMZ are shown in Fig. S1. All the ceramics exhibited pure perovskite structures (ABO_3) with symmetry changing with BMZ content. BCT20 ceramics exhibited a tetragonal phase, evidenced by the split {200} peaks, consistent with the previous study on Ca-doped $BaTiO_3$ ceramics[30]. Ceramics with BMZ content higher than 10% exhibit a pseudocubic phase with single {200} and {111} peaks. It was reported that the overall structure was transformed from tetragonal to pseudocubic when sufficient amount of $BiMO_3$ was introduced in $BaTiO_3$-$BiMO_3$ binary systems[15]. The lattice volume increases with BMZ content, as shown in Fig. 1a, attributed to ionic radius differences between $(Ba_{0.8}Ca_{0.2})^{2+}$ (1.56 Å) and Bi^{3+} (1.38 Å), and between Ti^{4+} (0.605 Å) and $(Mg_{0.5}Zr_{0.5})^{3+}$ (0.72 Å)[31], with BO_6 octahedra dominating the perovskite unit cell volume[32]. Temperature-dependent dielectric constant (ε_r) curves at 1 kHz for the ceramics are compared in Fig. 1b and the temperature-dependent dielectric properties under various frequencies are given in Fig. S2. The BCT20 ceramics exhibited relatively sharp and temperature-sensitive dielectric peaks at around 130 °C, corresponding to its Curie point, which is consistent with the previous study[30]. When BMZ is introduced, frequency dispersion of dielectric properties indicates relaxor characteristics[11]. The relaxor characteristics can be evaluated by the diffuseness degree of phase transition, by fitting the dielectric data using modified Curie-Weiss law: $1/\varepsilon_r - 1/\varepsilon_m = (T - T_m)^\gamma/C$, where ε_m is the maximum dielectric constant and T_m is the corresponding temperature[33]. As shown in Fig. S3, the γ value of BCT20 ceramics is 1.2, indicating the ferroelectric-like phase transition. All other ceramics show γ value greater than 1.5, demonstrating diffuse phase transition which is a typical relaxor feature. T_m shifted to higher temperatures with increasing BMZ content, as evidenced in Fig. 1b, which is also observable in other BT-based relaxors[16,19,34]. The relaxor characteristics are reflected in the *P-E* loops. As shown in Fig. 1c, BCT20 ceramics exhibited hysteretic *P-E* loops due to ferroelectric characteristics, while the ceramics with BMZ endmember show slim *P-E* loops due to disrupted long-range ordering and disordered local fields.

Energy storage properties (W_{rec} and η) are obtained by integrating the *P-E* loop, as illustrated in Fig. S4. To comprehensively evaluate the energy storage performance, a parameter $W_F = W_{rec}/(1-\eta)$ was defined[35] and the W_F values for these ceramics at 200 kV/cm are compared in Fig. 1d, where the 70BCT20-30BMZ composition possesses the highest W_F value, indicating it has both a high W_{rec} and a high η. The comprehensive energy storage performance was attributed to the dense microstructure, low dielectric loss, and strong relaxor characteristics, as evidenced in Figs. S2, S3, S5, S6. Based on these characterizations, 70BCT20-30BMZ was chosen for detailed studies to assess its potentials in energy storage applications.

The comprehensive energy storage performance of 70BCT20-30BMZ ceramics is primarily attributed to the high-entropy engineering. As depicted in Fig. S7, the configuration entropy S_{config}, calculated using Eq. (1), gradually increases with BMZ concentration, with compositions $x \geq 0.2$ falling into the high-entropy region[21]. It was reported that the significant lattice distortion associated with high-entropy effects enhances the likelihood of collisions between electrons and atoms, resulting in lower conductivity and higher energy storage performance[24]. As shown in Fig. S8, the tolerance factor decreases monotonically with BMZ content increasing. The room-temperature and high-temperature energy storage properties of 70BCT20-30BMZ ceramics will be discussed in the following sections.

Room-temperature energy storage properties of high-entropy engineered 70BCT20-30BMZ ceramics

The *P-E* loops of 70BCT20-30BMZ ceramics at room temperature under various electric fields are displayed in Fig. 2a. This *P-E* loops remain slim shape even under a high electric field of 720 kV/cm, leading to both high W_{rec} of 10.9 J/cm^3 and high η of 93%. The reproducibility of the energy storage properties is satisfying, exhibiting similar values with minimal variation across different samples, as shown in Fig. S9. The energy storage performance of 70BCT20-30BMZ is superior to most of the reported lead-free relaxor ceramics whose energy efficiencies are greater than 90%[18,25,36–53], as illustrated in Fig. 2b. The outstanding energy storage performance is related to its strong relaxor characteristics and high breakdown strength (BDS), as shown in Figs. S7a, b. The high BDS of 70BCT20-30BMZ ceramics is associated with its large bandgap, as shown in Figs. S7c, d, which means that the electrons are hard to jump across the bandgap and contribute to the conduction, leading to a low leakage current, especially at high electric field. The lower BDS observed in the sample with $x = 0.4$ can be attributed to weak inter-grain adhesion, evidenced by the intergranular fracture feature in Fig. S11. The lower BDS of the ceramic with $x = 0.2$ may be linked to needle-like secondary phases, as shown in Fig. S5c. The secondary phases are also influenced by the high-entropy design, as evidenced by a significant reduction in their concentration as the BMZ content increases to 30%, indicating that the entropy plays a crucial role in the dissolution for the secondary phases within the solid solutions and enhances the perovskite phase stability. As shown in Fig. S12, the ceramic also exhibited outstanding charge-discharge characteristics, where 90% of the stored energy can be released to the 1 kΩ load resistor within 250 ns, leading to a high power density of 24.4 MW/cm^3. The slight difference between the energy density calculated from *P-E* loops (7.4 J/cm^3 at 550 kV/cm) and charge-discharge curves (6.8 J/cm^3 at 550 kV/cm) arises from the different time scales of the two measurements[54].

Cyclic *P-E* measurements were performed at 450 kV/cm and repeated up to 10^6 cycles. The calculated W_{rec} and η as functions of cycle number are shown in Fig. 2c. After 10^6 cycles, the energy storage performance exhibited negligible change, with $\Delta W_{rec} < 0.2\%$ and $\Delta\eta < 0.1\%$, demonstrating its ultrahigh cycling reliability. To investigate the cycling reliability, local structures of the ceramics were examined by scanning transmission electron microscopy (STEM) before and after cyclic measurements. The high-angle annular dark-field (HAADF) images of the sample before and after 10^6 electric field cycles are displayed in Fig. 2d, e, respectively. The displacements of B-site cations in the corresponding unit cells were marked by arrows, illustrated in Fig. S13. Most regions in both HAADF images are dark blue, indicating the displacement magnitudes of B-site cations are small before and after the cycling measurement. Nevertheless, nano polar regions (PNRs) can still be observed in the two samples, which are closely related to the relaxor characteristics[11,55]. The PNRs did not coalesce to form micro polar regions even after being exposed to a high electric

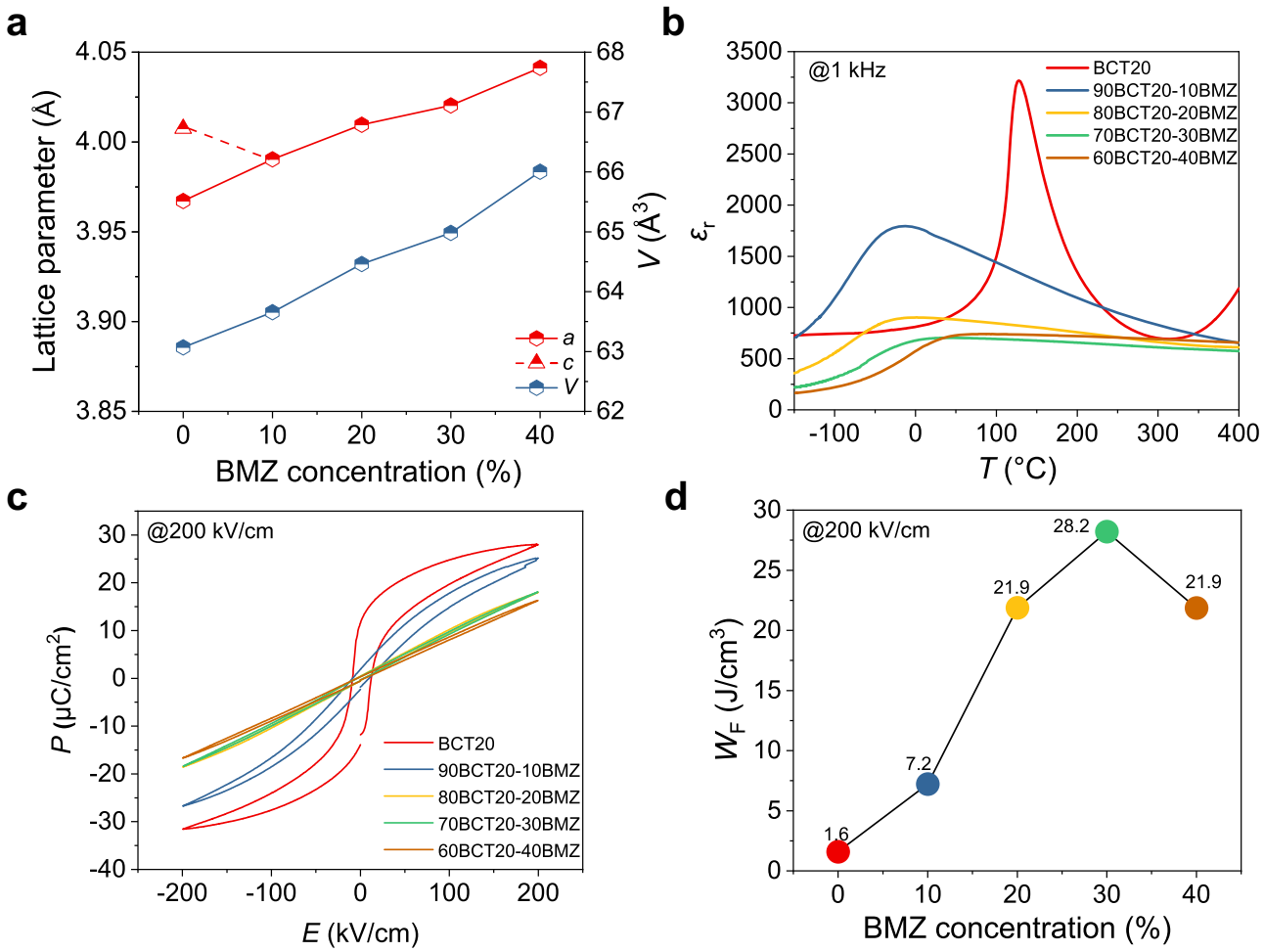

Fig. 1 | Comparison of the structural and electrical properties of (100-100*x*) BCT20-100*x*BMZ ceramics. a The variations of lattice parameters and volume as a function of BMZ content. **b** The change of dielectric constant (ε_r) at 1 kHz as a function of temperature for the studied ceramics. **c** The *P-E* loops at 200 kV/cm of the ceramics. **d** The calculated W_F parameter for the ceramics with different BMZ contents. The number near the symbol represents the W_F value of the corresponding composition.

https://doi.org/10.1038/s41467-025-56195-0

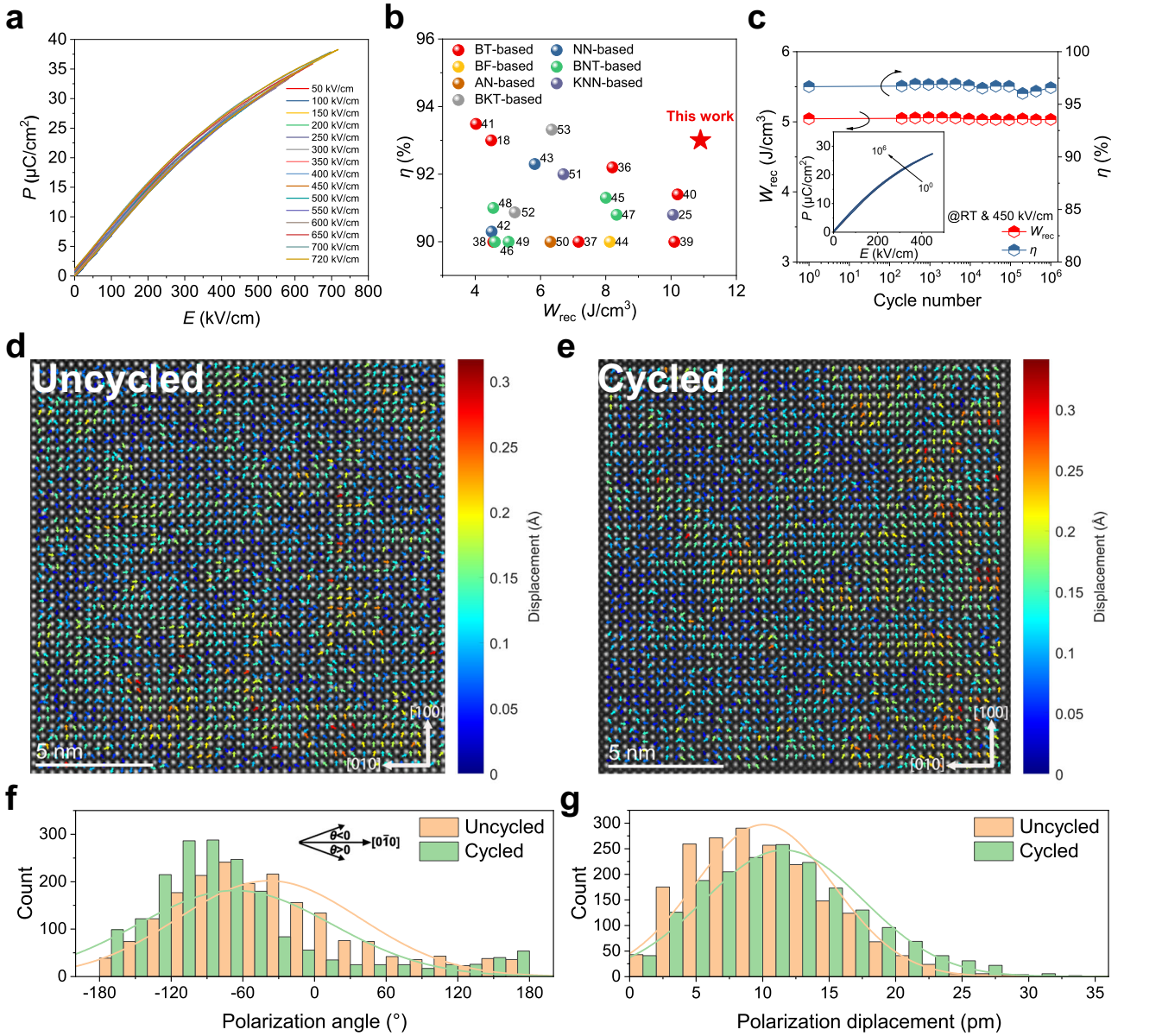

Fig. 2 | Room-temperature energy storage performance of 70BCT20-30BMZ ceramics and their local structures. a *P-E* loops under various electric fields. **b** Comparison of the energy storage performance between 70BCT20-30BMZ ceramic and other lead-free relaxor ceramics whose $\eta > 90\%$. The number near the symbol represents the corresponding reference number. **c** The cycling reliability measured at 450 kV/cm up to 10^6 cycles. The inset shows the *P-E* loops after various cycles. **d**–**e** Atomic-resolution HAADF-STEM images recorded along the crystallographic [001] direction for the ceramics before and after 10^6 cycles under 450 kV/cm, respectively. The arrow direction and color denote the projections of the displacement direction and magnitude, respectively, of B-site cation in the corresponding unit cell. **f**–**g** Distribution of polarization vector angle and displacement amplitude before and after cycling, respectively.

field of 450 kV/cm for 10^6 times, demonstrating their high dynamic under repeated electric fields. The distributions of polarization angles and displacements are shown in Fig. 2f, g, respectively, showing slight changes in both distributions before and after 10^6 cycles. The nanoscale microstructures also exhibited high stability after 10^6 cycles, as shown in Fig. S14. Therefore, the PNRs with high electric-field stability prevented from forming large domains which is associated with the remnant polarization and hysteresis in *P-E* loops, leading to high energy efficiency and ultra-stable energy storage performance during cycling measurements.

High-temperature energy storage performance of high-entropy 70BCT20-30BMZ ceramics

Motivated by the highly dynamic PNRs and ultra-stable cycling stability of energy storage performance, we investigated the high-temperature energy storage performance of 70BCT20-30BMZ. The energy storage W_{rec} and η measured at 450 kV/cm as a function of temperature is presented in Fig. 3a. The ceramic exhibited stable energy storage performance ($\Delta W_{rec} < 9\%$ and $\Delta\eta < 5\%$) over a wide temperature range of −50 °C to 260 °C. Notably, η remains above 90% even at 250 °C, indicating both dielectric loss and conductivity are minimal at the measurement conditions. The temperature range T_{90} where η exceeds 90%, is compared with other ceramics[18,37,44,45,50,56–58] in Fig. 3b. Although 70BCT20-30BMZ ceramic exhibits lower room-temperature W_{rec} compared to the ceramics prepared by repeated rolling process (RRP)[56,57], the temperature range T_{90} is wider than them, demonstrating its comprehensive high-temperature energy storage performance. For practical high-temperature applications, the reliability at high temperature environment is important. The energy storage properties and the *P-E* loops measured at 200 °C and repeated electric field of

https://doi.org/10.1038/s41467-025-56195-0

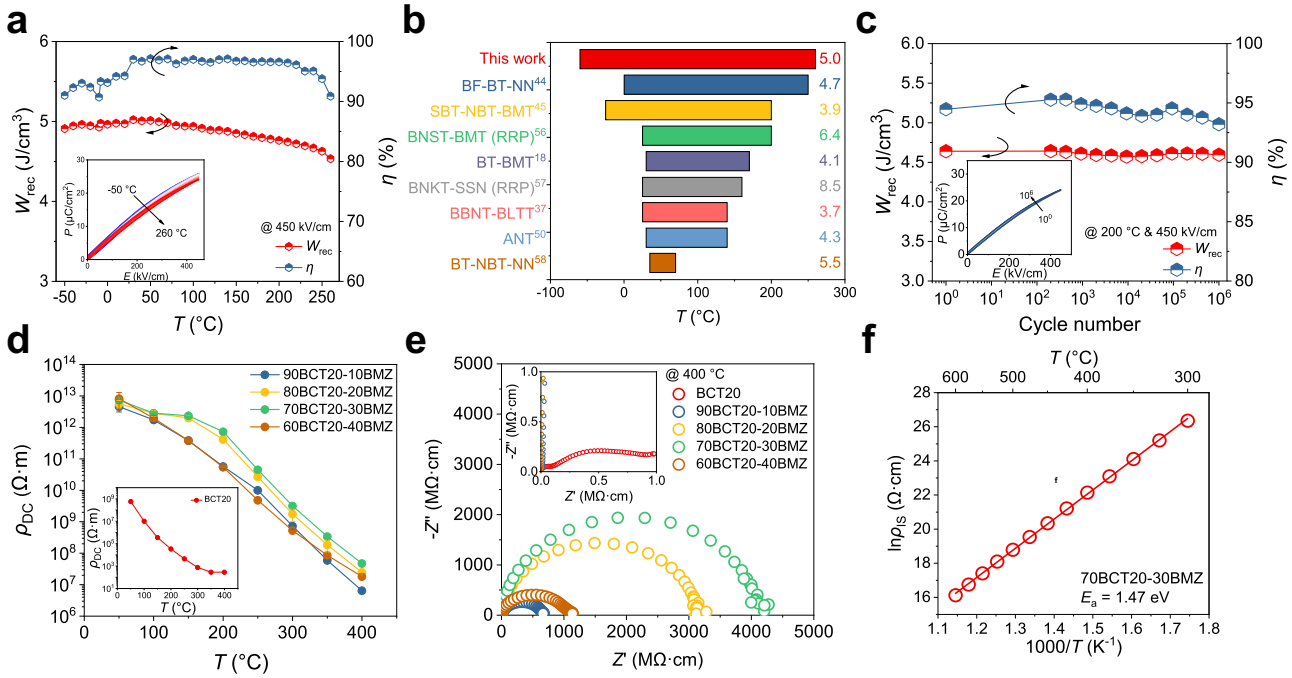

Fig. 3 | High-temperature energy storage performance of 70BCT20-30BMZ ceramics. a W_{rec} and η as functions of measurement temperature. The inset shows the *P-E* loops at different temperatures. **b** The temperature range in which $\eta > 90\%$ for 70BCT20-30BMZ ceramics and other relaxor ceramics. The number near each bar represents the room-temperature W_{rec}. **c** The cycling reliability was measured at 450 kV/cm and 200 °C up to 10^6 cycles. The inset shows the *P-E* loops after various cycles. **d** Variations of DC resistivity (ρ_{DC}) with temperature for (100-100*x*) BCT20-100*x*BMZ ceramics. The error bars represent the standard deviation. **e** Impedance complex plots of (100-100*x*)BCT20-100*x*BMZ ceramics at 400 °C. **f** Arrhenius plot of the bulk resistivity (ρ_{IS}) of 70BCT20-30BMZ ceramics.

450 kV/cm are shown in Fig. 3c and the inset, respectively. The *P-E* loops remain unchanged after 10^6 cycles, leading to stable W_{rec} and η with variations less than 0.9% and 1.3%, respectively, revealing a superior reliability at elevated temperature up to 200 °C.

The excellent high-temperature energy storage performance is attributed to the high resistivity (ρ) and high activation energy for conductivity (E_a) of the 70BCT20-30BMZ ceramics. Variations in DC resistivities (ρ_{DC}) with temperature for (100-100*x*)BCT20-100*x*BMZ ceramics are shown in Fig. 3d. Compared to the compositions with BMZ endmember, BCT20 ceramics exhibited lower DC resistivity due to the incompact microstructure, as shown in Fig. S5a. When BMZ endmember was introduced, the DC resistivity of ceramics was improved significantly, reaching 10^{12} Ω·m at room temperature. Consequently, the resistivity and BDS of the high-entropy compositions ($0.2 \le x \le 0.4$) are higher than those of medium-entropy ($x = 0.1$) and low-entropy ($x = 0$) compositions. Of particular importance is that the ceramics still exhibit high ρ_{DC} at high temperatures, especially the composition with $x = 0.3$ shows the largest value among the ceramics, which is curcial for high-temperature applications. The high-temperature insulation properties can also be characterized by impedance measurement. As shown in Fig. 3e, the BCT20 ceramics displayed two distinct semicircles in the impedance complex plot at 400 °C: a smaller semicircle in the high-frequency region, attributed to grain responses, and a larger semicircle in the low-frequency region, corresponding to grain boundary responses. In contrast, all other ceramics exhibited a single semicircle under the same measurement conditions, indicating a response solely from the grain boundaries. With the BMZ concentration increasing, the bulk resistivity (ρ_{IS}) of the ceramics at 400 °C determined by the intersect point of impedance curve and *Z'* axis, increases first then decreases. The highest bulk resistivity was achieved in 70BCT20-30BMZ, consistent with the results obtained in DC resistivity measurements. The bulk resistivities of 70BCT20-30BMZ ceramic were extracted from the impedance curves measured at various temperatures, and the Arrhenius plot is given in Fig. 3f. The calculated activation energy for conductivity is 1.47 eV, almost half of the optical bandgap of the ceramic, indicating that the conduction mechanism is intrinsic conduction. The enhanced electrical homogeneity is also responsible for improving the BDS by reducing the interface polarization[59,60]. As shown in Fig. S15, the frequency difference between *Z''-f* peak and *M''-f* peak is reduced when BMZ content increases from 0 to 30%, indicating the distribution of electric field is more uniform and hence the higher BDS in 70BCT20-30BMZ ceramics. Another important figure-of-merit (FOM) for high-temperature capacitors is *RC* constant, which is a measure of both the insulation and capacitance at a given temperature[61]. Moreover, *RC* constant is geometry independence because it is in fact the product of dielectric constant and resistivity of the material, making it possible to characterize and compare various families of dielectrics. The comparison of *RC* constant between 70BCT20-30BMZ ceramics and other dielectric ceramics as shown in Table S1 and Table S2. Regardless of at 200 °C and 300 °C, the RC constant of 70BCT20-30BMZ ceramic is superior to that of other dielectric ceramics, demonstrating its great potential for high-temperature capacitor applications.

In-situ structural characterizations for high-entropy 70BCT20-30BMZ ceramics

To investigate the structures of 70BCT20-30BMZ ceramics under high temperatures and electric fields, in-situ characterization techniques including TEM, XRD, and Raman spectroscopy were performed, with results are presented in Fig. 4. It has been reported that PNRs in relaxor materials can be transformed into large ferroelectric domains under high electric fields[62,63], thereby impacting the electrical properties. Of particular interest is that the 70BCT20-30BMZ ceramics, even under an ultrahigh electric field of ~1000 kV/cm, do not witness the significant introduction of large ferroelectric domains, as observed in Fig. 4a, b. Furthermore, applying a constant electric field of ~400 kV/cm, heating the sample up to 250 °C did not visibly alter the microstructure, as shown in Fig. 4c, d. Hence, the PNRs in 70BCT20-30BMZ

https://doi.org/10.1038/s41467-025-56195-0

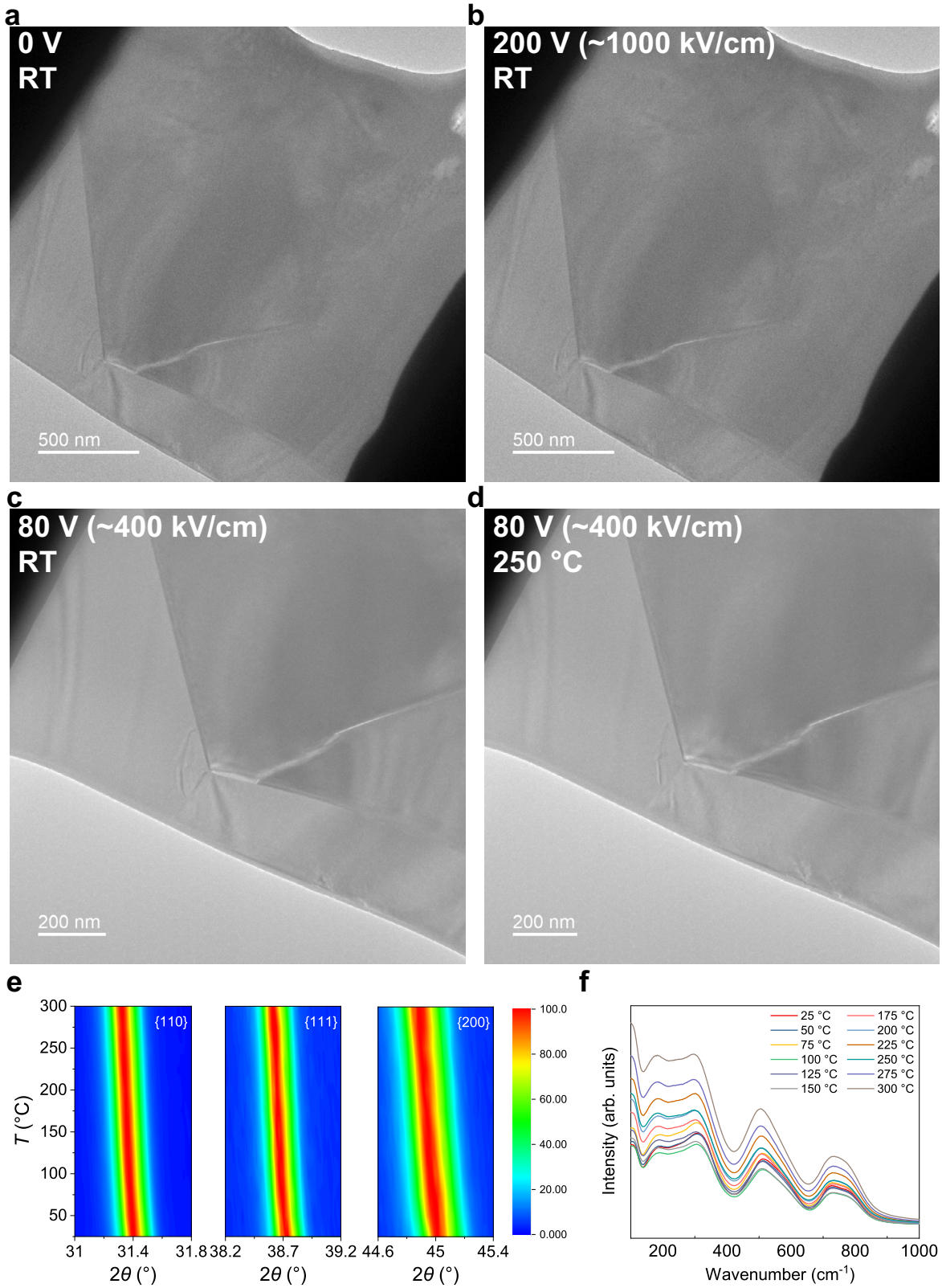

Fig. 4 | In-situ characterizations for 70BCT20-30BMZ ceramics. a–**b** TEM images recorded at room temperature and under 0 V and 200 V, respectively. The black parts on top left and bottom right are Pt electrodes. **c**–**d** TEM images recorded under 80 V and at room temperature and 250 °C, respectively. **e** The enlarged {110}, {111}, and {200} diffraction peaks under various temperature. The intensities were normalized. **f** Raman spectra measured under various temperature.

ceramics exhibit high dynamic under both high temperatures and electric fields without coalescing into large domains, being consistent with observations from *P-E* loops measured at various temperatures and repeated electric fields.

Additionally, the XRD patterns of 70BCT20-30BMZ measured under different temperatures are shown in Fig. S16. The ceramics exhibited a pseudocubic phase without phase transition over the temperature range of 25 to 300 °C, as evidenced by the absence of

peak splitting or distortion for {110}, {111}, and {200} peaks in Fig. 4e. The slight shifts of peaks towards lower angles suggests lattice expansion within this temperature range. The calculated expansion coefficient approximately $9 \sim 10 \times 10^{-5}$ /°C, aligns with the thermal expansion coefficient of cubic $BaTiO_3$[6], indicating that the lattice expansion in 70BCT20-30BMZ ceramics is primarily due to thermal expansion rather than phase transitions. Similarly, no new peaks or peaks splitting are observed in Raman spectra shown in Fig. 4f, signifying that no phase transition in the same temperature range. Overall, as revealed by these in-situ characterizations, the structure of 70BCT20-30BMZ demonstrates robust thermal and electrical stability, which is attributed to the large lattice distortion and random local fields induced by the high-entropy engineering. This stability underpins the excellent performance of these ceramics in energy storage applications at both room temperature and high temperatures.

In summary, (100-100x)BCT20-100xBMZ ($x = 0 \sim 0.4$) ceramics were synthesized and characterized, with configuration entropy increasing with x. Thoroughly considering W_{rec} and η, high-entropy composition 70BCT20-30BMZ was selected for in-depth studies. This composition exhibits both a high W_{rec} of 10.9 J/cm^3 and a high η of 93%, along with excellent cycling reliability at room temperature. Of particular importance is that 70BCT20-30BMZ ceramics also showed excellent high-temperature stability with $\Delta W_{rec} < 9\%$ and $\Delta\eta < 5\%$ over a broad temperature range of −50 °C to 260 °C, meanwhile exhibiting superior cycling reliability with minimal property degradation after cycling at 450 kV/cm and 200 °C. Electrical and in-situ characterizations revealed the PNRs in the ceramics are highly dynamic under varying temperatures and electric fields, attributed to the high-entropy engineering. This dynamic PNRs underscores the excellent high-temperature energy storage performance and high cycling reliability. This research highlights the significant potential of 70BCT20-30BMZ ceramics for high-temperature capacitors, and demonstrates that high-entropy design is an effective strategy in developing high-performance dielectric materials.

Methods

Ceramic preparation

High purity (> 99.9%) oxides and carbonate $BaCO_3$, $CaCO_3$, Bi_2O_3, TiO_2, ZrO_2, and MgO (all from Aladdin) were weighed according to the chemical formula (1-x)($Ba_{0.8}Ca_{0.2}$)TiO_3-xBi($Mg_{0.5}Zr_{0.5}$)O_3 ($x = 0$, 0.1, 0.2, 0.3, and 0.4, abbreviated as (100-100x)BCT20-100xBMZ) and ball milled in anhydrous ethanol with yttrium-stabilized zirconia (YSZ) balls for 12 h. The slurries were dried and calcined at 850 °C for 2 h with a heating rate of 5 °C/min. Afterwards, the calcined powders were ball milled again for 24 h to reduce the particle size. The powders were mixed with 0.2 wt% Rhoplex binder and ball milled for 2 h. The powders with binder were sieved and uniaxially pressed into 10-mm-diameter pellets under 30 MPa, followed by cold isostatically pressed under 200 MPa for 2 min. The binder was burned out by heating the pellets at 600 °C for 2 h with a heating rate of 2 °C/min. The pellets were sintered at 1000–1300 °C (the higher the BMZ content, the lower the sintering temperature) for 2 h to achieve dense ceramics. The sintered ceramics were thinned and polished to achieve parallel surfaces. Fire-on silver pastes or sputtered gold films were used as electrodes for measurements.

Phase and microstructure characterizations

The phase purity and lattice parameters were determined by powder X-ray diffraction (D8 Advance, Bruker) on ground sintered ceramic pellets. The microstructures of the ceramics were observed by a field-emission scanning electron microscope (FE-SEM) (Merlin Compact, Zeiss). Before SEM observations, the ceramics were polished and thermally etched at 150 °C below the corresponding sintering temperature for 15 min. The average grain size and standard deviation were calculated from 200 measured grain size data. Transmission Electron Microscopy (TEM) specimens were prepared by a dual-beam Focused Ion Beam (FIB, Helios 5 UC, ThermoFisher Scientific). The target cutting areas in ceramics were first deposited with tungsten protection layers with a thickness of 2 μm, and then the surrounding regions were removed by accelerated Ga ions. The specimens were bonded on commercial Cu grids and then thinned down by Ga ions with accelerating voltage and beam current of 30 kV and 2.5 nA, and finally 2 kV and 40 pA were used for the precise removal of surface amorphous layers. The thicknesses of investigation areas were about 30–40 nm. A double spherical aberration (C_s) corrected scanning transmission electron microscopy (STEM, Spectra 300, Thermo Fisher Scientific) operated at 300 kV was employed to characterize the atomic-scale structures, chemical compositions. The convergence angle in STEM mode and high-angle annular dark-field (HAADF) acceptance angles were 25 mrad and 39–200 mrad, respectively. Electron diffraction patterns, bright-field (BF) and dark-field (DF) images were acquired in 200 kV TEM (Talos F200X, Thermo Fisher Scientific) using centered dark field technique. Target areas were tilted to [001] zone axes to obtain diffraction patterns, and then (100) and (110) diffraction spots were caught using objective aperture for DF imaging.

Spectrum measurements

The optical absorption properties of polished ceramics were measured in the wavelength range of 200–800 nm using a UV-VIS-NIR spectrometer (Lambda 1050 + , PerkinElmer). The optical bandgaps (E_g) were calculated based on Tauc formula $(\alpha h\nu)^2 = B(h\nu\text{-}E_g)$, where α is the optical absorption coefficient, h is Planck constant, ν is the light frequency, and B is a fitting constant. The Raman spectra were recorded by a Raman spectrometer (HR800, HORIBA) using a 532-nm laser excitation without polarization. The resolution of Raman spectrometer is 1 cm^{-1}.

Dielectric, impedance, and resistivity measurements

The dielectric constant (ε_r) and loss (tanδ) were measured as functions of temperature and frequency by an impedance analyzer (E4990A, Keysight) combined with a temperature control stage (HFSE91-PB2, Linkam). The impedance spectroscopy measurements were performed an impedance gain-phase analyzer (1260, Solartron) equipped with a dielectric interface (1296, Solartron). The resistivity was measured by an electrometer (6517B, Keithley). The average resistivity and deviation were calculated from 350 measured resistivity data.

Ferroelectric, breakdown, and charge-discharge measurements

The ferroelectric measurements (P-E loop measurements) were performed by a ferroelectric tester (TF 1000, AixACCT). The breakdown measurements were performed by a dielectric breakdown measurement system (PK-CPE1701, PolyK). The breakdown voltages were recorded by applying a dc voltage with a ramping rage of 500 V/s until the sample broke down. Weibull distribution ($P(E_i) = 1 - \exp(-E_i/E_b)^\beta$) was used to characterize the BDS of the ceramics. $P(E_i)$ is the cumulative breakdown probability of a certain electric field, E_i is the BDS of each sample. E_b and β are the Weibull characteristic BDS and Weibull modulus, respectively. The charge-discharge measurements were performed by a capacitor charge-discharge measurement system (PK-CRP1701, PolyK) using a 1 kΩ load resistor. Thin samples with thickness around 50 μm were used for the above measurements.

Reporting summary

Further information on research design is available in the Nature Portfolio Reporting Summary linked to this article.

Data availability

All the data used to generate figures in this paper are provided in the Source Data file. Source data are provided with this paper.

References

1. Sarjeant, W. J., Zirnheld, J. & MacDougall, F. W. Capacitors. *IEEE Trans. Plasma Sci.* **26**, 1368–1392 (1998).
2. Furman, E. et al. High-temperature, high-power capacitors: the assessment of capabilities. *SAE Int. J. Aerosp.* **1**, 822–831 (2008).
3. Li, H. et al. Dielectric polymers for high-temperature capacitive energy storage. *Chem. Soc. Rev.* **50**, 6369–6400 (2021).
4. Zeb, A. & Milne, S. J. High temperature dielectric ceramics: a review of temperature-stable high-permittivity perovskites. *J. Mater. Sci: Mater. Electron* **26**, 9243–9255 (2015).
5. Li, Q. et al. High-temperature dielectric materials for electrical energy storage. *Annu Rev. Mater. Res.* **48**, 219–243 (2018).
6. Jaffe B., Cook W. R., Jaffe H. *Piezoelectric Ceramics*. Academic Press (1971).
7. Yang, L. et al. Perovskite lead-free dielectrics for energy storage applications. *Prog. Mater. Sci.* **102**, 72–108 (2019).
8. Wang, G. et al. Electroceramics for high-energy density capacitors: current status and future perspectives. *Chem. Rev.* **121**, 6124–6172 (2021).
9. Yao, Z. et al. Homogeneous/inhomogeneous-structured dielectrics and their energy-storage performances. *Adv. Mater.* **29**, 1601727 (2017).
10. Wang, J. & Shen, Z.-H. Modeling-guided understanding microstructure effects in energy storage dielectrics. *Microstructures* **1**, 2021006 (2021).
11. Li, F., Zhang, S., Damjanovic, D., Chen, L.-Q. & Shrout, T. R. Local structural heterogeneity and electromechanical responses of ferroelectrics: learning from relaxor ferroelectrics. *Adv. Funct. Mater.* **28**, 1801504 (2018).
12. Zhou, L., Vilarinho, P. M. & Baptista, J. L. Dependence of the structural and dielectric properties of $Ba_{1-x}Sr_xTiO_3$ ceramic solid solutions on raw material processing. *J. Eur. Ceram. Soc.* **19**, 2015–2020 (1999).
13. Shvartsman, V. V., Zhai, J. & Kleemann, W. The dielectric relaxation in solid solutions $BaTi_{1-x}Zr_xO_3$. *Ferroelectrics* **379**, 77–85 (2009).
14. Lei, C., Bokov, A. A. & Ye, Z. G. Ferroelectric to relaxor crossover and dielectric phase diagram in the $BaTiO_3$–$BaSnO_3$ system. *J. Appl Phys.* **101**, 084105 (2007).
15. Beuerlein, M. A. et al. Current understanding of structure-processing-property relationships in $BaTiO_3$-$Bi(M)O_3$ dielectrics. *J. Am. Ceram. Soc.* **99**, 2849–2870 (2016).
16. Ogihara, H., Randall, C. A. & Trolier-McKinstry, S. Weakly coupled relaxor behavior of $BaTiO_3$-$BiScO_3$ ceramics. *J. Am. Ceram. Soc.* **92**, 110–118 (2009).
17. Yang, L., Kong, X., Cheng, Z. & Zhang, S. Ultra-high energy storage performance with mitigated polarization saturation in lead-free relaxors. *J. Mater. Chem. A* **7**, 8573–8580 (2019).
18. Hu, Q. et al. Achieve ultrahigh energy storage performance in $BaTiO_3$–$Bi(Mg_{1/2}Ti_{1/2})O_3$ relaxor ferroelectric ceramics via nanoscale polarization mismatch and reconstruction. *Nano Energy* **67**, 104264 (2020).
19. Raengthon, N., Sebastian, T., Cumming, D., Reaney, I. M. & Cann, D. P. $BaTiO_3$-$Bi(Zn_{1/2}Ti_{1/2})O_3$-$BiScO_3$ ceramics for high-temperature capacitor applications. *J. Am. Ceram. Soc.* **95**, 3554–3561 (2012).
20. Oses, C., Toher, C. & Curtarolo, S. High-entropy ceramics. *Nat. Rev. Mater.* **5**, 295–309 (2020).
21. Sarkar, A. et al. High-entropy oxides: fundamental aspects and electrochemical properties. *Adv. Mater.* **31**, 1806236 (2019).
22. Yang, B. et al. High-entropy enhanced capacitive energy storage. *Nat. Mater.* **21**, 1074–1080 (2022).
23. Qi, J. et al. High-entropy assisted $BaTiO_3$-based ceramic capacitors for energy storage. *Cell Rep. Phys. Sci.* **3**, 101110 (2022).
24. Yang, B. et al. Engineering relaxors by entropy for high energy storage performance. *Nat. Energy* **8**, 956–964 (2023).
25. Chen, L. et al. Giant energy-storage density with ultrahigh efficiency in lead-free relaxors via high-entropy design. *Nat. Commun.* **13**, 3089 (2022).
26. Zhang, S. High entropy design: a new pathway to promote the piezoelectricity and dielectric energy storage in perovskite oxides. *Microstructures* **3**, 2023003 (2023).
27. Chen, L. et al. Large energy capacitive high-entropy lead-free ferroelectrics. *Nano-Micro Lett.* **15**, 65 (2023).
28. Gao, Y. et al. Optimizing high-temperature energy storage in tungsten bronze-structured ceramics via high-entropy strategy and bandgap engineering. *Nat. Commun.* **15**, 5869 (2024).
29. Peng, H. et al. High-entropy relaxor ferroelectric ceramics for ultrahigh energy storage. *Nat. Commun.* **15**, 5232 (2024).
30. Mitsui, T. & Westphal, W. B. Dielectric and x-ray studies of $Ca_xBa_{1-x}TiO_3$ and $Ca_xSr_{1-x}TiO_3$. *Phys. Rev.* **124**, 1354–1359 (1961).
31. Shannon, R. D. Revised effective ionic radii and systematic studies of interatomic distances in halides and chalcogenides. *Acta Crystallogr A* **32**, 751–767 (1976).
32. Yuan, Q. et al. Simultaneously achieved temperature-insensitive high energy density and efficiency in domain engineered $BaTiO_3$-$Bi(Mg_{0.5}Zr_{0.5})O_3$ lead-free relaxor ferroelectrics. *Nano Energy* **52**, 203–210 (2018).
33. Uchino, K. & Nomura, S. Critical exponents of the dielectric-constants in diffused-phase-transition crystals. *Ferroelectrics* **44**, 55–61 (1982).
34. Huang, C.-C. & Cann, D. P. Phase transitions and dielectric properties in $Bi(Zn_{1/2}Ti_{1/2})O_3$–$BaTiO_3$ perovskite solid solutions. *J. Appl Phys.* **104**, 024117 (2008).
35. Pan, H. et al. Ultrahigh energy storage in superparaelectric relaxor ferroelectrics. *Science* **374**, 100–104 (2021).
36. Guo, J. et al. Achieving excellent energy storage properties in fine-grain high-entropy relaxor ferroelectric ceramics. *Adv. Electron. Mater.* **8**, 2200503 (2022).
37. Chen, X. et al. Tailoring phase fraction induced saturation polarization delay for high-performance $BaTiO_3$-based relaxed ferroelectric capacitors. *ACS Appl Mater. Interfaces* **15**, 40735–40743 (2023).
38. Yang, H. et al. Novel $BaTiO_3$-based, Ag/Pd-compatible lead-free relaxors with superior energy storage performance. *ACS Appl Mater. Interfaces* **12**, 43942–43949 (2020).
39. Sun, Z. et al. Superior capacitive energy-storage performance in Pb-free relaxors with a simple chemical composition. *J. Am. Chem. Soc.* **145**, 6194–6202 (2023).
40. Xiao, W. et al. Free energy regulation and domain engineering of $BaTiO_3$-$NaNbO_3$ ceramics for superior dielectric energy storage performance. *Chem. Eng. J.* **461**, 142070 (2023).
41. Shi, C. et al. Significantly enhanced energy storage performances and power density in (1 − *x*)BCZT-*x*SBT lead-free ceramics via synergistic optimization strategy. *Chem. Eng. J.* **426**, 130800 (2021).
42. Wei, T. et al. Novel $NaNbO_3$–$Sr_{0.7}Bi_{0.2}TiO_3$ lead-free dielectric ceramics with excellent energy storage properties. *Ceram. Int* **47**, 3713–3719 (2021).
43. Kang, R. et al. Extraordinary energy storage performance and thermal stability in sodium niobate-based ceramics modified by the ion disorder and stabilized antiferroelectric orthorhombic R phase. *J. Mater. Chem. A* **9**, 24387–24396 (2021).
44. Qi, H., Xie, A. W., Tian, A. & Zuo, R. Z. Superior energy-storage capacitors with simultaneously giant energy density and efficiency using nanodomain engineered $BiFeO_3$-$BaTiO_3$-$NaNbO_3$ lead-free bulk ferroelectrics. *Adv. Energy Mater.* **10**, 1903338 (2020).
45. Wang, Z. et al. Achieving ultrahigh energy-storage density with excellent thermal stability in $Sr_{0.7}Bi_{0.2}TiO_3$-based relaxors via polarization behavior modulation. *ACS Appl Mater. Interfaces* **14**, 44389–44397 (2022).

46. Joseph, J., Cheng, Z. & Zhang, S. $NaNbO_3$ modified $BiScO_3$-$BaTiO_3$ dielectrics for high-temperature energy storage applications. *J. Materiomics* **8**, 731–738 (2022).
47. Li, D. et al. Lead-free relaxor ferroelectric ceramics with ultrahigh energy storage densities via polymorphic polar nanoregions design. *Small* **19**, 2206958 (2023).
48. Ye, H. et al. Significantly improvement of comprehensive energy storage performances with lead-free relaxor ferroelectric ceramics for high-temperature capacitors applications. *Acta Mater.* **203**, 116484 (2021).
49. Li, D. et al. Enhanced energy storage properties achieved in $Na_{0.5}Bi_{0.5}TiO_3$-based ceramics via composition design and domain engineering. *Chem. Eng. J.* **419**, 129601 (2021).
50. Luo, N. et al. Constructing phase boundary in $AgNbO_3$ antiferroelectrics: pathway simultaneously achieving high energy density and efficiency. *Nat. Commun.* **11**, 4824 (2020).
51. Li, D. et al. Improved energy storage properties achieved in (K, Na) NbO_3-based relaxor ferroelectric ceramics via a combinatorial optimization strategy. *Adv. Funct. Mater.* **32**, 2111776 (2021).
52. Niu, Z. et al. $Bi_{0.5}K_{0.5}TiO_3$-based lead-free relaxor ferroelectric with high energy storage performances via the grain size and bandgap engineering. *Mater. Today Chem.* **24**, 100898 (2022).
53. Zheng, L. et al. Simultaneously achieving high energy storage performance and remarkable thermal stability in $Bi_{0.5}K_{0.5}TiO_3$-based ceramics. *Mater. Today Energy* **28**, 101078 (2022).
54. Li, J. et al. Grain-orientation-engineered multilayer ceramic capacitors for energy storage applications. *Nat. Mater.* **19**, 999–1005 (2020).
55. Liu, G., Chen, L. & Qi, H. Energy storage properties of $NaNbO_3$-based lead-free superparaelectrics with large antiferrodistortion. *Microstructures* **3**, 2023009 (2023).
56. Li, D. et al. A high-temperature performing and near-zero energy loss lead-free ceramic capacitor. *Energy Environ. Sci.* **16**, 4511–4521 (2023).
57. Zhao, W. et al. Broad-high operating temperature range and enhanced energy storage performances in lead-free ferroelectrics. *Nat. Commun.* **14**, 5725 (2023).
58. Chen, L. et al. Local diverse polarization optimized comprehensive energy-storage performance in lead-free superparaelectrics. *Adv. Mater.* **34**, e2205787 (2022).
59. Wang, G. et al. Ultrahigh energy storage density lead-free multilayers by controlled electrical homogeneity. *Energy Environ. Sci.* **12**, 582–588 (2019).
60. Wang, C., Cao, W., Liang, C., Zhao, H. & Wang, C. Equimolar high-entropy for excellent energy storage performance in $Bi_{0.5}Na_{0.5}TiO_3$-based ceramics. *Energy Storage Mater.* **70**, 103534 (2024).
61. Jia, W. et al. Advances in lead-free high-temperature dielectric materials for ceramic capacitor application. *IET Nanodielectrics* **1**, 3–16 (2018).
62. Qu, W., Zhao, X. & Tan, X. Evolution of nanodomains during the electric-field-induced relaxor to normal ferroelectric phase transition in a Sc-doped $Pb(Mg_{1/3}Nb_{2/3})O_3$ ceramic. *J. Appl Phys.* **102**, 084101 (2007).
63. Fan, Z. & Tan, X. Dual-stimuli in-situ TEM study on the nonergodic/ergodic crossover in the $0.75(Bi_{1/2}Na_{1/2})TiO_3$–$0.25SrTiO_3$ relaxor. *Appl Phys. Lett.* **114**, 212901 (2019).

Acknowledgements

C.-W.N. and Y.-H. Lin acknowledged the support of National Natural Science Foundation of China (Grant No. 52388201). X.K. acknowledged the support of National Natural Science Foundation of China (Grant No. 52302276) and China Postdoctoral Science Foundation (Grant No. 2022M721763). L.Y. acknowledged the support of National Natural Science Foundation of China (Grant No. 52302277) and State Key Laboratory of New Ceramic Materials Tsinghua University (Grant No. KF202401).

Author contributions

The work was conceived and designed by X.K., L.Y., and C.-W.N. X.K. and L.Y. prepared the samples and characterized the structural, spectrum, dielectric, impedance, resistivity, ferroelectric, breakdown, and charge-discharge measurements, and processed the related data. J.G., F.M., T.Z., and H.Z. performed the TEM characterizations and data analyzes. The manuscript was drafted by X.K. and revised by L.Y., Y.-H.L, H.H., S.Z., J.G. and C.-W.N. All authors participated in the data analysis and discussions.

Competing interests

The authors declare no competing interests.

Additional information

Supplementary information The online version contains supplementary material available at https://doi.org/10.1038/s41467-025-56195-0.

Correspondence and requests for materials should be addressed to Letao Yang, Jinming Guo or Ce-Wen Nan.

Peer review information *Nature Communications* thanks Abdul Manan, Maqbool Ur Rehman and Abd El-razek Mahmoud for their contribution to the peer review of this work. A peer review file is available.